



*Supplement of*

## **Massive sediment pulses triggered by a multi-stage 130 000 m<sup>3</sup> alpine cliff fall (Hochvogel, DE–AT)**

**Natalie Barbosa et al.**

*Correspondence to:* Natalie Barbosa ([barbosa@biologie.uni-muenchen.de](mailto:barbosa@biologie.uni-muenchen.de))

The copyright of individual parts of the supplement might differ from the article licence.

## 1. Multi-temporal quantification of surface change

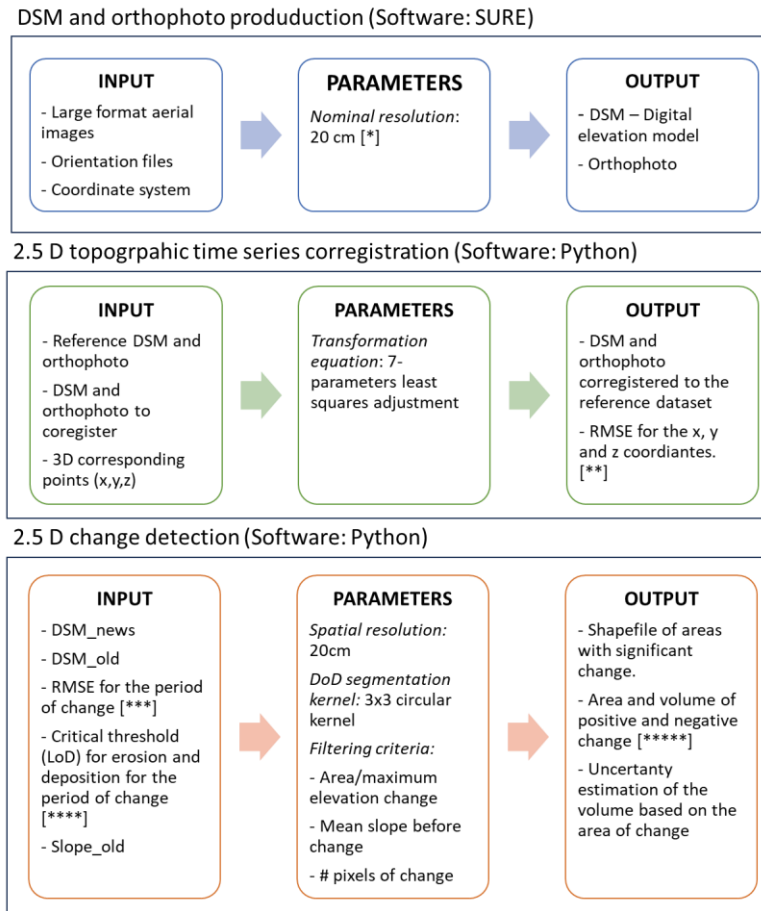


**Figure S1.** Summary of the methodological steps followed for the calculation of volumes of change in steep terrain. [\*] The nominal resolution of the DSM and orthophotos is determined by the height of the flight defined by the surveying agency. [\*\*]

- 5 The RMSE (root mean square error) is a useful metric to reveal systematic errors and estimate the uncertainty between two datasets. [\*\*\*] We calculate the RMSE for each dataset, i.e., each DoD combination, as a measure of error and use it for the error propagation. [\*\*\*\*] The critical threshold (LoD following Wheaton et al., 2010) is determined for each process, i.e., erosion (negative change) and deposition (positive change) and each morphological zone that account for the topographic and shadowing influence on the photogrammetric reconstruction. [\*\*\*\*\*] The volumes of change are calculated only for areas of significant change according to the critical thresholds.
- 10

The workflow proposed for the calculation of volumes of changes in steep terrains using large format high-resolution aerial imagery results from the combination of previously published methodologies, i.e., semi-global matching algorithm (Hirschmüller, 2008), 7-parameter 3D similarity transformation (Akca, 2010), topographic change detection (James et al., 2012; Wheaton et al., 2010), and geomorphic sediment budget (Wheaton et al., 2010a), and the implementation of intermediate steeps, i.e., DoD segmentation and filtering of ‘false rockfalls’ based on morphometric characteristics, differential critical error, and volume error estimation based on the RMSE between the two surveys of interest. The intermediate steps respond to the particularities of large format high-resolution aerial imagery acquired by different governmental survey agencies without the purpose of change detection analysis and the limitation of nadir-view acquisition to accurately map steep terrain. A summary of the methodological step is presented in Fig. S1. Further research is need to better determine the significant change

15

20

and the uncertainty on the volume calculation of erosion and deposition on areas with steep and inhomogeneous terrain.

### 1.1. Datasets

25

We used large format aerial imagery surveyed by the Bundesamt für Eich- und Vermessungswesen (BEV); the Landesamt für Digitalisierung, Breitband und Vermessung (LDBV); and the company 3D RealityMaps. Detail information on the aerial surveys is listed in Table S1.

30 **Table S1.** Detail information on the aerial surveys. Bundesamt für Eich- und Vermessungswesen (BEV). Landesamt für Digitalisierung, Breitband und Vermessung (LDBV)

Year	Source	Date	Coverage (km <sup>2</sup> )	Image overlap	Resolution (cm)	Camera (focal length mm)	
2009	LDBV	29.07.2009	36	80:50	20	UltraCam-(100.5)	X
2010	BEV	12.09.2010	48	80:60	20	UltraCam-Xp (100.5)	
2012	LDBV	20.08.2012	45	80:50	20	UltraCam-(100.5)	XP
2014	BEV	23.09.2014	48	80:60	20	UltraCam-Eagle M1 (100.5)	
2015	LDBV	30.06.2015, 01.07.2015	55	80:50	20	UltraCam (100.5)	XP
2017	BEV	07.08.2017	125.10	80:60	20	UltraCam-Eagle M1 (100.5)	
<b>2018</b>	<b>3DRM</b>	<b>20.9.2018</b> <b>21.9.2018</b>	<b>48</b>	<b>80:70</b>	<b>10</b>	<b>UltraCam-Eagle M2 (100.5)</b>	
2020	LDBV	27.07.2020, 28.07.2020, 21.08.2020, 04.09.2020	55.77	80:50	20	UltraCam-Eagle M3 (100.5)	

### 1.2. 3D-coregistration evaluation

The 3D-coregistration successfully align the datasets within a spatial uncertainty close to the spatial resolution. Table S2 summarizes the metrics used to later estimate the critical thresholds for change detection.

35

**Table S2.** Assessment of the 3D-coregistration for each dataset.

Time periods of change	N points	RMSE (m)	RMSE X (m)	RMSE Y (m)	RMSE Z (m)
2010	25	0.203	0.074	0.086	0.168
2012	19	0.203	0.078	0.102	0.157
2014	13	0.211	0.118	0.132	0.113
2015	17	0.197	0.072	0.086	0.162
2017	30	0.191	0.103	0.091	0.133
2018			Reference		
2020	27	0.136	0.064	0.047	0.11

Additionally, we independently evaluate the elevation uncertainty after the 3D-coregistration using additional 30 independent well-distributed points on stable areas with a complex topography and close to the area of interest.

40 The location of the points is presented in Fig. S2. The elevation uncertainty, measured as the RMSE of the elevation difference in stable areas with complex topography, ranges from 30 to 40 cm depending on the combination of datasets. The combination used for this publication is summarized in Table S3.

**Table S3.** Elevation uncertainty

45

Time periods of change	Z_RMSE
2010-2012	0.343
2012-2014	0.335
2014-2015	0.296
2015-2017	0.375
2017-2018	0.382
2018-2020	0.297

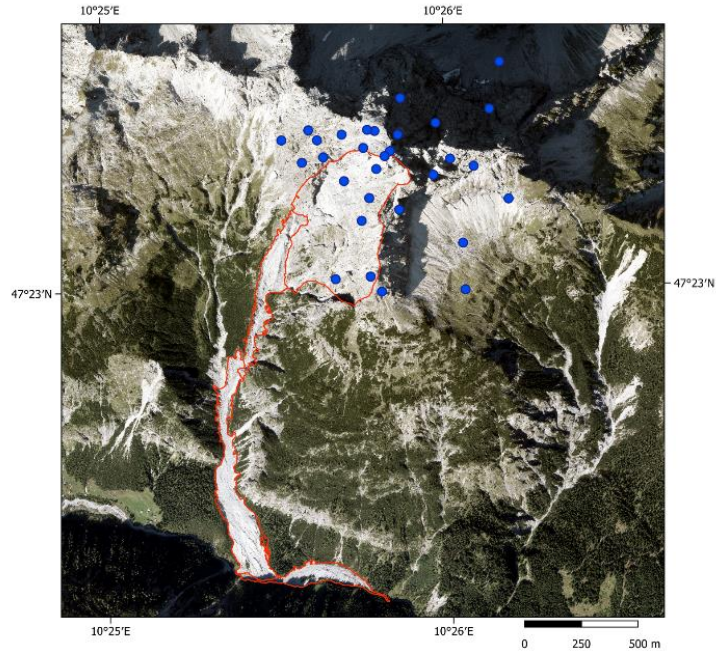


**Figure S2.** Distribution of points to assess the elevation uncertainty after the 3D-coregistration. We decided to focus on the upper slope because is the area with the highest theoretical uncertainty due to topography complexity.

### 1.3. Critical thresholds

#### 1.3.1. Frequency-magnitude curves

The polygons interpreted as primary and secondary rockfalls used for the construction of the decadal frequency-magnitude curves are based on the segmentation according to the critical thresholds determined by best practice and summarized in Table S4.

**Table S4.** Critical threshold in meters for the four slopes that constitute the Hochvogel summit.

	<b>northern slope</b>	<b>western slope</b>	<b>southwestern slope</b>	<b>southeastern slope</b>
Erosion (m)	1	1	1	1
Deposition (m)	0.33	0.5	0.6	0.6

#### 1.3.2. Cascading geomorphic sediment budgets

A sediment budget describes the input, transport, storage, and export of sediment in a geomorphic system. This concept provides an effective basis for representing the key components of the sediment delivery system within a catchment and for assembling the necessary data to elucidate, understand and predict catchment sediment delivery (Walling and Collins, 2008) and estimate related natural hazards. The geomorphic sediment budget (Wheaton et al., 2010a) is calculated as the sum of the masked DoD values of erosion (negative change) and deposition (positive change).

$$Q_{b_{in}} - Q_{b_{out}} = \frac{\Delta V_{DoD}}{\Delta t} \quad (1)$$

$$\Delta V_{DoD} = \sum V_{deposition} - \sum V_{erosion} \quad (2)$$

70 where  $Q_{bin}$  is the sediment produced,  $Q_{bout}$  is the sediment eroded, and  $\Delta V_{DoD}$  the change in storage in a given  
 timestamp calculated by Eq. (2). If  $\Delta V_{DoD}$  is positive, there is aggradation. If the  $\Delta V_{DoD}$  is negative, there is  
 degradation.

For each region and time interval, a critical threshold for erosion and deposition was determined by best practice  
 75 and summarized in Table S5.

**Table S5.** Critical threshold in meters for each region and time interval.

Time interval	rock face		upper channelized debris flow channel		widened disperse debris flow channel		outlet	
	Erosion (m)	Deposition (m)	Erosion (m)	Deposition (m)	Erosion (m)	Deposition (m)	Erosion (m)	Deposition (m)
2010-2012	-1	0.33	-0.6	0.34	-0.6	0.4	-0.22	0.22
2012-2014	-0.8	0.34	-0.6	0.33	-0.4	0.4	-0.2	0.2
2014-2015	-0.4	0.8	-0.8	0.8	-0.45	0.3	-0.4	0.2
2015-2017	-1	0.6	-1	0.6	-0.4	0.5	-0.2	0.2
2017-2018	-1.2	0.4	-0.8	0.4	-0.4	0.4	-0.2	0.2
2018-2020	-0.3	0.6	-0.3	0.6	-0.3	0.6	-0.2	0.2

#### 1.4. 2016 cliff fall event

80 The volume inside a manually delimited extent of the cliff fall resulted in a mean of 142 047 m<sup>3</sup> and a standard  
 deviation of 3475 m<sup>3</sup> thus an uncertainty of 2.4% from the total volume. This uncertainty percentage is used in  
 decadal analysis of rockfall at the slopes that constitute the Hochvogel summit knowing that the 2016 cliff fall  
 corresponds to the coalescence of at least 6 individual detachments The volume calculated for all possible  
 combinations of time intervals is summarized in Table S6.

85 **Table S6.** 2.5. volume calculation of the cliff fall occurred in 2016 for each possible time-stamp combination. The calculation  
 has been done based on a polygon delimitation.

2017 combinations	Volume (m <sup>3</sup> )	2018 combinations	Volume (m <sup>3</sup> )	2020 combinations	Volume (m <sup>3</sup> )
2017-2009	-139 326	2018-2009	-136 328	2020-2009	-140 535
2017-2010	<b>-147 471</b>	2018-2010	<b>-144 201</b>	2020-2010	<b>-148 759</b>
2017-2012	-140 738	2018-2012	-137 940	2020-2012	-141 992
2017-2014	-141 892	2018-2014	-138 697	2020-2014	-143 123
2017-2015	-144 085	2018-2015	-140 842	2020-2015	-145 364

A field visit to the outlet to the Jochbach river took place the 14.07.2022. The continuous river erosion is documented in Fig. S3. Field observations are consistent with geomorphic changes presented on the temporal series of DoDs (Fig.7 main manuscript).



90

**Figure S3.** Field observations at the outlet (geomorphic zone D). Picture taken from the river channel on 14.07.2022.

## 2. Multi-stage detachment analysis

We estimate the seismic volumes following the methodology described in Le Roy et al., 2019. They determined a relation between seismic energy  $E_s$  caused by a rock fall and its initial potential energy  $E_p$  expressed by Eq. 3:

$$E_s = aE_p^b \quad (3)$$

$$\text{with } a = 10^{-8} \text{ and } b = 1.55$$

With this relation, the source volume can be calculated by Eq. 4:

$$V = \frac{E_s^{\frac{1}{b}}}{agpH} \quad (4)$$

100

where  $g$  is the gravity constant ( $9.81 \text{ m s}^{-2}$ ),  $p$  is the density of the rock fall material and  $H$  is the fall height of the fallen block.

We calculated the seismic Energy  $E_s$  following the equations 5,6 and 7, in Le Roy et al., 2019:

$$E_s = 2\pi r p h c \int_{t_0}^{t_1} u_{env}(t)^2 e^{\alpha t} \varepsilon dt \quad (5)$$

105

$$u_{env}(t) = \sqrt{u(t)^2 + H(u(t)^2)} \quad (6)$$



$$u(t) = \sqrt{u^2_E(t) + u^2_N(t) + u^2_Z(t)} \quad (7)$$

with  $r$  being the distance between seismic station and rock fall impact,  $h$  being the thickness of the layer through which the surface waves traveled,  $c$  being the velocity of the seismic waves,  $t_0$  and  $t_1$  being the start and end times of the impact signal,  $u_{\text{env}}(t)$  being the envelope of the ground velocity  $u(t)$  determined via the Hilbert transform  $H$ ,  
 110  $\alpha$  being an attenuation factor accounting for the inelastic attenuation of the waves and  $\varepsilon$  being a site effect coefficient.

## 2.1. Seismic stations

We used 7 seismic broadband stations from the Austrian and Bavarian earthquake observatories listed in Table S7.

115 **Table S7.** Seismic stations. Abbreviation of sensor type according to `eseis` package (Dietze, 2018).

ID	name	x	y	z	sensor_type	network
OBER	Oberstdorf	597 551	5 251 204	896	LE3D5S	BW <sup>1</sup>
PART	Partenkirchen	659 143	5 262 560	760	LE3D5S	BW <sup>1</sup>
ZUGS	Zugspitze	649 280	5 253 292	2650	L4C	BW <sup>1</sup>
DAVA	Damuels	566 566	5 237 400	1602	STS2	OE <sup>2</sup>
MOTA	Moosalm	658 900	5 245 627	1575	STS2	OE <sup>2</sup>
RETA	Reutte	632 755	5 260 801	965	STS2	OE <sup>2</sup>
A037A	Verwall	595 994	5 213 757	2020	TC120s	Z3 <sup>3</sup>

<sup>1</sup> Department of Earth and Environmental Sciences, Geophysical Observatory, University of Muenchen. (2001) via <http://erde.geophysik.uni-muenchen.de/fdsnws/station/1/query?>

<sup>2</sup> ZAMG - Zentralanstalt für Meteorologie und Geodynamik. (1987) via <http://www.orfeus-eu.org/fdsnws/station/1/query?>

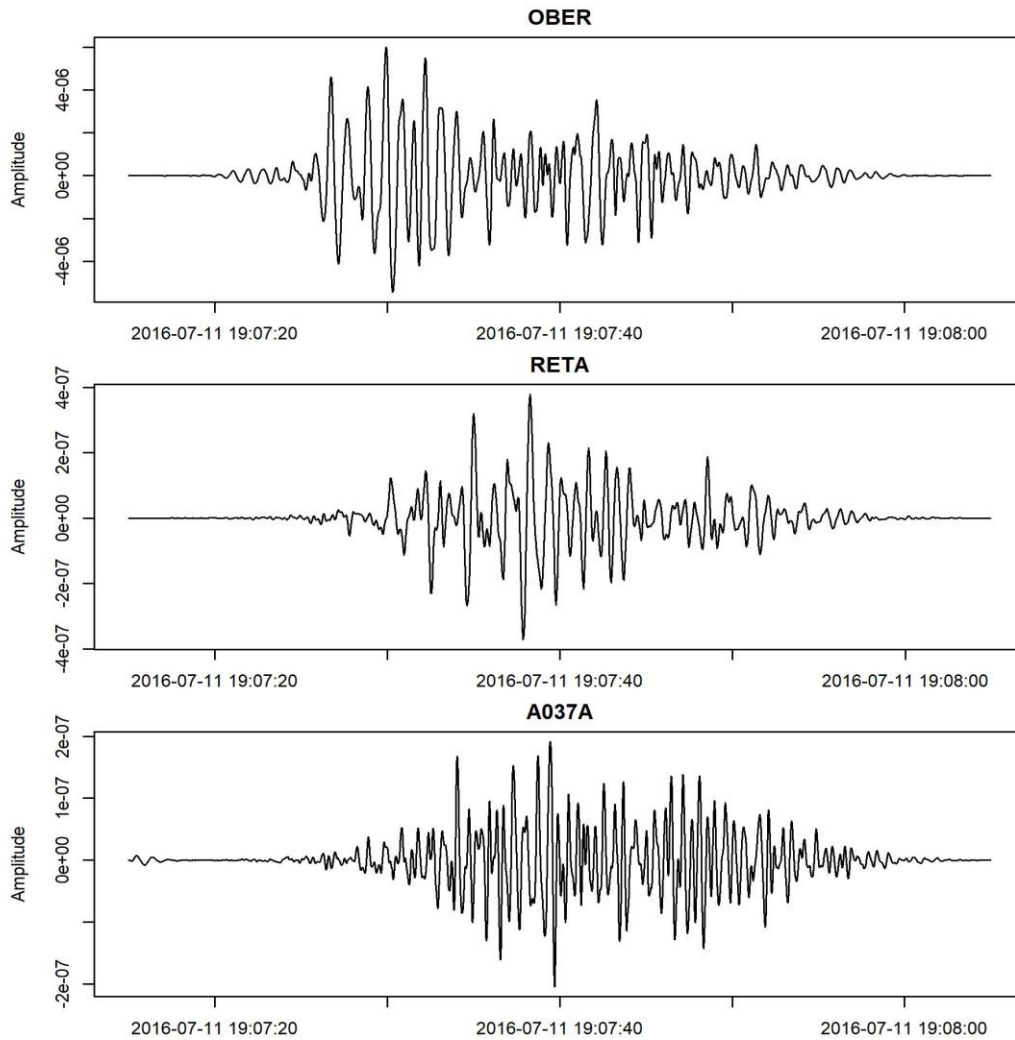
120 <sup>3</sup> *AlpArray Seismic Network (2015)* via <https://erde.geophysik.uni-muenchen.de/fdsnws/datasetselect/1/query?>

## 2.2. Event detection

Using the knowledge of rockfall activity at the Hochvogel flank between July 9<sup>th</sup> and 11<sup>th</sup> 2016, we examined the seismic signals of all stations during this time period. By analyzing the local seismic amplitude and the  
 125 corresponding spectrograms at each station, we identified all seismic events with the strongest impact at the closest station in Oberstdorf. Rock falls produce a seismic impact over all frequencies between 5 and 50 Hz (Le Roy et al., 2019); We only included events where there is a clear decrease in seismic intensity with increasing distance of the stations from the Hochvogel (strongest in OBER, then RETA, then DAVA) and significant arrival time differences of up to 20 s (first in OBER, then RETA, then A037A, then DAVA) (Fig. S4). We excluded  
 130 earthquakes based on distinct arrivals of P and S waves, a lower frequency content, and small signal arrival times differences between the stations. Most earthquakes could also be linked to an event in the regional and global



135 earthquake event records. Local anthropogenic noise could be identified by higher frequency contents and missing coincidence of the signals between different stations. Following these criteria, we identified all seismic signals potentially originating from the rock fall series at the Hochvogel. We assured the origination of the seismic events at the Hochvogel due to the fact that all signals decay with increasing distance of the station from the Hochvogel, the overall similar arrival time delay patterns, and their coincidence to personal rock fall activity observations by hikers during the analyzed time period.



140 **Figure S4.** Seismograms of a rockfall. The intensity of the seismic energy decreases and arrival times increase with increasing distance of the stations from the Hochvogel (strongest in OBER, then RETA, then A037A).

**Table S8.** Summary of the rockfalls identified between 9<sup>th</sup> and 11<sup>th</sup> of July

event	First arrival time at OBER in UTC	status
1	2016-07-09 08:37:45	probably rock fall signal
2	2016-07-09 17:39:27	probably rock fall signal
3	2016-07-11 17:39:36	probably rock fall signal

4	2016-07-11 18:48:13	clearly rock fall signal
5	2016-07-11 19:05:19	clearly rock fall signal
6	2016-07-11 19:07:16	clearly rock fall signal

The latest three seismic events show clear evidence for originating from the Hochvogel rock failure, while the first three events are harder to constrain due to their smaller amplitude. Nevertheless, these also show the same intensity decay and arrival time patterns at the closest stations and can therefore be taken into account. For the parameter estimation, we only used the clear events [4,5,6] in Table S8.

### 2.3. Parameter estimation

#### *r (distance)*

The distance of the seismic stations to the source rock fall at the Hochvogel has been calculated as topography corrected distance using *spatial\_migrate()* from the *eseis* package (Dietze, 2018) The results are listed in Table S9.

**Table S9.** Distance of each seismic station from the Hochvogel.

ID	distance (m)
OBER	11 783
PART	54 696
ZUGS	41 344
DAVA	43 173
MOTA	53 916
RETA	27 433
A037A	39 224

#### *p (density)*

We assume a ground density of the carbonate rock to  $2500 \pm 100 \text{ kg m}^{-3}$ .

#### *c (velocity)*

The main seismic energy is transported by the surface waves and not the fastest P-waves. We, therefore, estimated the relevant seismic velocity based on the timing of the peak ground velocity and peak envelope value at each station (vertical component) filtered between 1 and 2 Hz (to avoid timely differences and distortion in higher frequencies). The velocity is found by the linear regression of the time difference and the distance difference for each station pair as  $1715 \pm 99 \text{ m s}^{-1}$  (Figure S5).

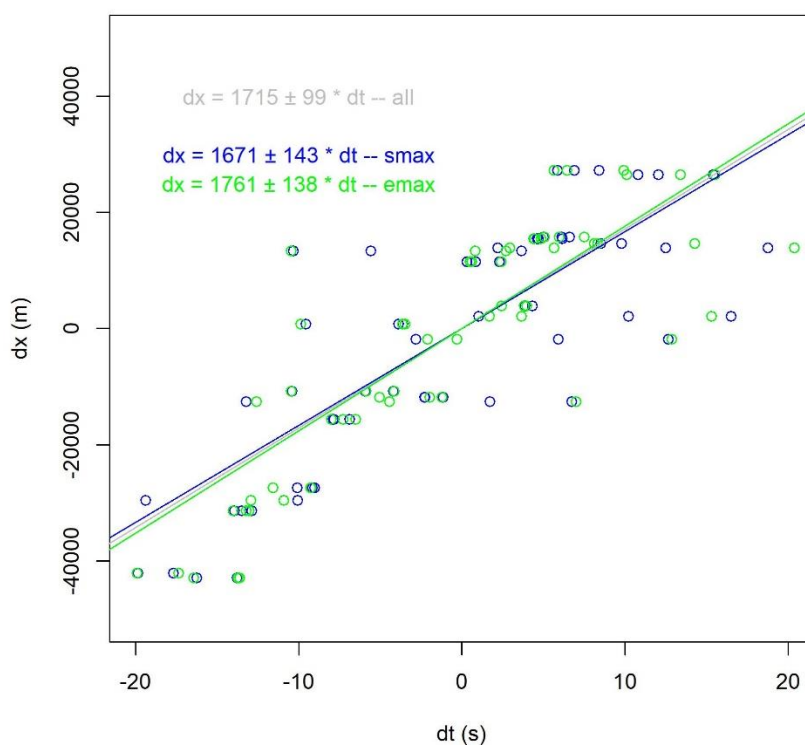


**Figure S5.** Linear regression for the estimation of the parameter  $c$  (velocity)

***h (thickness of layer)***

The centroid frequency ( $f_{\text{centroid}}$ ) of the seismic signals is  $4.93 \pm 0.92$  Hz (calculated with *signal\_stats()* from *eseis*). We, therefore, estimated the thickness of the layer through which the surface waves travel as one Rayleigh wavelength with  $h = c/f_{\text{centroid}}$ .

***t0 and t1***

Onset and end times of seismic events have been picked manually from the filtered seismograms.

***u<sub>env</sub> (envelope)***

170 The envelope of the seismic signal has been calculated using the *signal\_envelope()* function from the *eseis* package.

***ε (site effect coefficient)***

We used the 10 strongest earthquakes of 2016 recorded by all stations (Table S10) to estimate the amplitude correction of each station relative to the OBER station (reference station,  $\epsilon = 1$ ).  $\epsilon$  has been set as the mean ratio  
 175 of peak signal envelope relative to OBER in the vertical component (filtered between 2 and 6 Hz containing the most energy around the frequency centroid). The results are listed in Table S11.

**Table S10.** Earthquakes used for the calculation of the parameter  $\varepsilon$  (site effect coefficient). Data source: USGS (2022)

Magnitude.	Location	Depth (km)	Origin time (UTC)	Region
7.9	4.505°S 153.522°E	94.5	2016-12-17 10:51:10	Kokopo, Papua New Guinea
7.8	42.737°S 173.054°E	15.1	2016-11-13 11:02:56	Amberley, New Zealand
7.8	0.382°N 79.922°W	20.6	2016-04-16 23:58:36	Muisne, Ecuador
7.8	4.952°S 94.330°E	24.0	2016-03-02 12:49:48	Sumatra, Indonesia
7.7	18.543°N 145.507°E	196.0	2016-07-29 21:18:24	Northern Mariana Islands
7.4	55.285°S 31.877°W	10.0	2016-08-19 07:32:22	South Georgia Island
7.2	22.477°S 173.117°E	16.4	2016-08-12 01:26:36	Loyalty Islands
7.2	56.241°S 26.935°W	78.0	2016-05-28 09:46:59	South Sandwich Islands
7.2	53.978°N 158.546°E	177.0	2016-01-30 03:25:12	Mil'kovo, Russia
7.1	0.046°S 17.826°W	10.0	2016-08-29 04:29:57	Ascension Island

**Table S11.** Summary of the estimated values for the parameter  $\varepsilon$  (site effect coefficient) for each seismic station.

ID	$\varepsilon$ (mean)	$\varepsilon$ (sd)
OBER	1.000000	0.0000000
PART	1.333635	0.4460248
ZUGS	2.870155	1.4927984
DAVA	3.032414	0.5136714
MOTA	3.730635	1.6229273
RETA	5.529136	1.1359063
A037A	3.086086	1.3231271

180  $\alpha$  (attenuation factor)

The attenuation factor has been estimated following the description of Le Roy et al. (2019) with a correction of the index  $i$  and  $j$  following Kanai et al. (1984) using the 3 rock fall events [4,5,6] and filtered vertical components between 2 and 6 Hz containing the most energy up to the frequency centroid:

$$\log_e \left[ \frac{a_i \varepsilon_j \left( \frac{r_i}{r_j} \right)^n}{a_j \varepsilon_i} \right] = -\alpha(r_i - r_j) \quad (8)$$

185 With  $\alpha$  being the amplitude of a station pair  $i$  and  $j$ ,  $n$  being 0.5 for surface waves and  $\alpha$  being the attenuation factor.  $\alpha$  has then been determined by a linear regression of the logarithm term and  $(r_i - r_j)$  (Fig. S6).

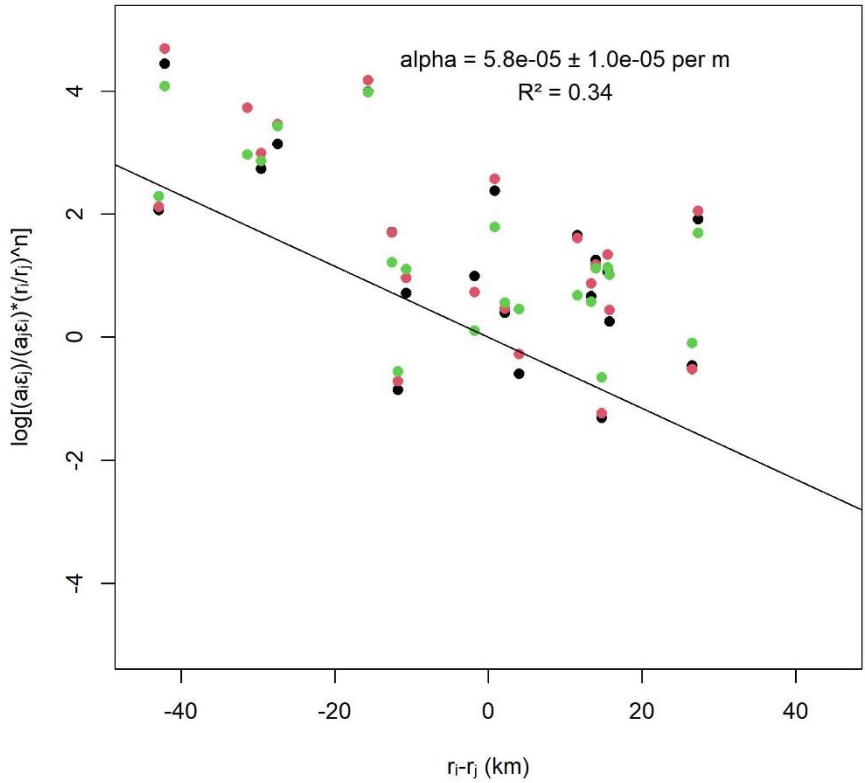


**Figure S6.** Linear regression for the estimation of the parameter  $\alpha$  (attenuation factor)

***H (fall height)***

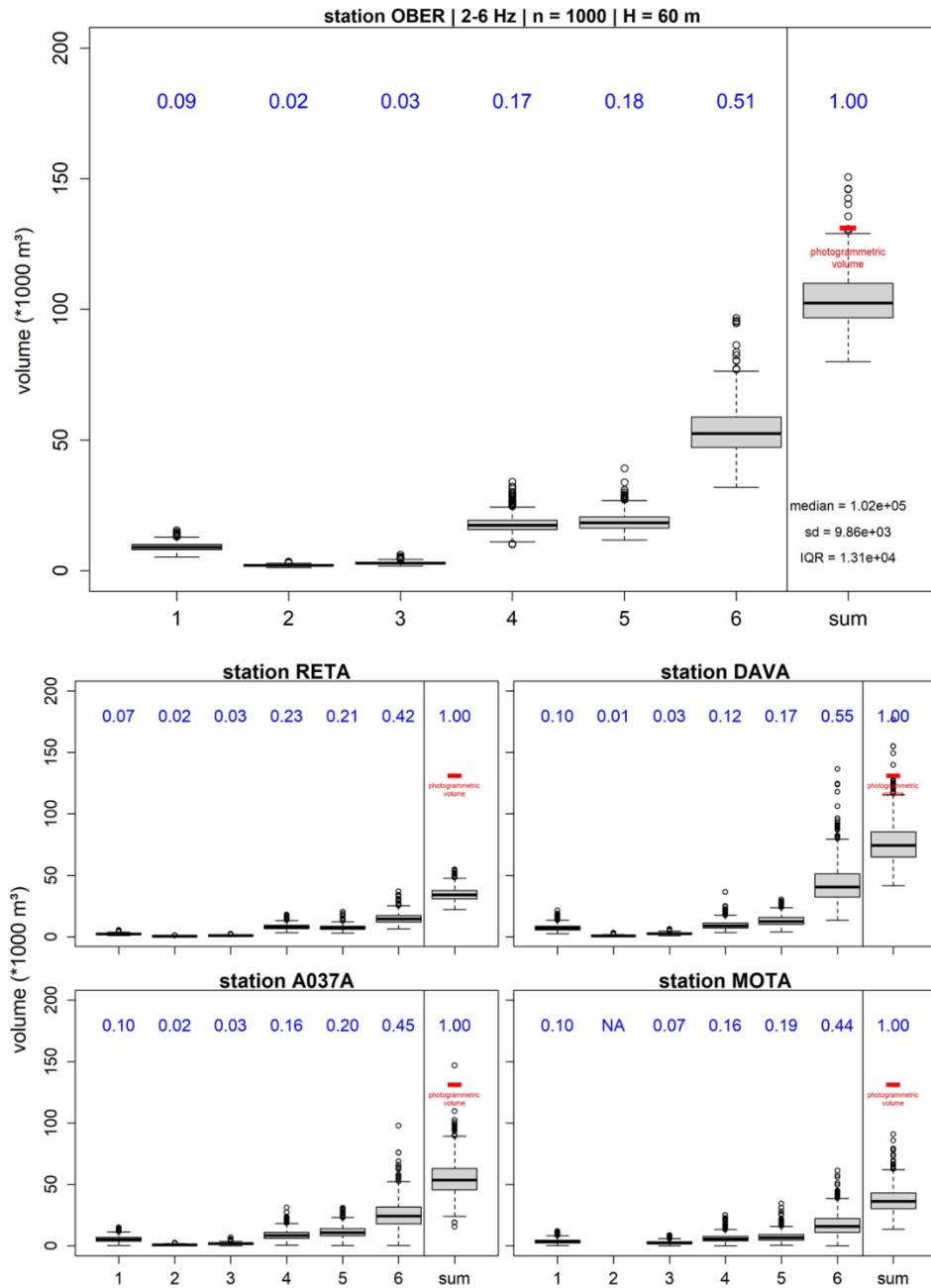
190 The fall height has been estimated by analyzing the 3D point clouds and DEM differences. A simple toppling of the center of gravity towards the slope corresponds to a fall height of 50-60 m while a sliding of the failed block suggests a probable fall height of 75 to 100 m.

2.4. Error estimation

195 All parameters have been estimated with a range or as mean with standard deviation. To estimate the error of the final volume calculation, we used 1000 iterations of a Monte Carlo simulation, where  $p$  is picked as a random deviate between the min and max values and  $c$ ,  $h$ ,  $\alpha$  and  $\epsilon$  are randomly generated values with the respective mean and standard deviation. This allows us to give a statistical range for the result of each sub-event at each station.

Additionally, we calculated the volume for all stations, although OBER is the closest station and therefore, the results are most reliable here.

The stations PART and ZUGS had to be excluded due to the bad signal-to-noise ratio of the rock fall signal. The volume estimation for each sub-event is summarized in Fig. S7 and Table S12.



205 **Figure S7.** Volume estimation for each sub-event (1 to 6 in x-axis) using a Monte-Carlo simulation with 1,000 iterations for each seismic station.

**Table S12.** Cumulative median total volume in m<sup>3</sup> for each seismic station for different fall heights.

	<b>OBER</b>		<b>RETA</b>		<b>DAVA</b>		<b>A037A</b>		<b>MOTA</b>		<b>MEAN</b>
fall height [m]	median	sd	median	sd	median	sd	median	sd	median	sd	
50	122,946	11,826	40,922	6,254	89,157	20,050	64,349	16,506	43,433	12,658	<b>72,161</b>
60	102,455	9,855	34,101	5,211	74,297	16,709	53,624	13,755	36,194	10,548	<b>60,134</b>
75	81,964	7,884	27,281	4,169	59,438	13,367	42,899	11,004	28,955	8,438	<b>48,107</b>
100	61,473	5,913	20,461	3,127	44,578	10,025	32,174	8,253	21,716	6,329	<b>36,081</b>

210

For all other stations, the respective sub-event's percentage of the total volume is very similar (Table S13). The stations further away than OBER underestimate the volume due to stronger signal damping, distortion, and worse coupling compared to the closest station OBER.

**Table S13.** Percentage (%) of the total volume per seismic station.

	<b>OBER</b>	<b>RETA</b>	<b>DAVA</b>	<b>A037A</b>	<b>MOTA</b>	<b>MEAN</b>
sub-event #1	9	7	10	10	10	9
sub-event #2	2	2	1	2	0	1
sub-event #3	3	3	3	3	7	4
sub-event #4	17	23	12	16	16	17
sub-event #5	18	21	17	2	19	19
sub-event #6	51	42	55	45	44	47

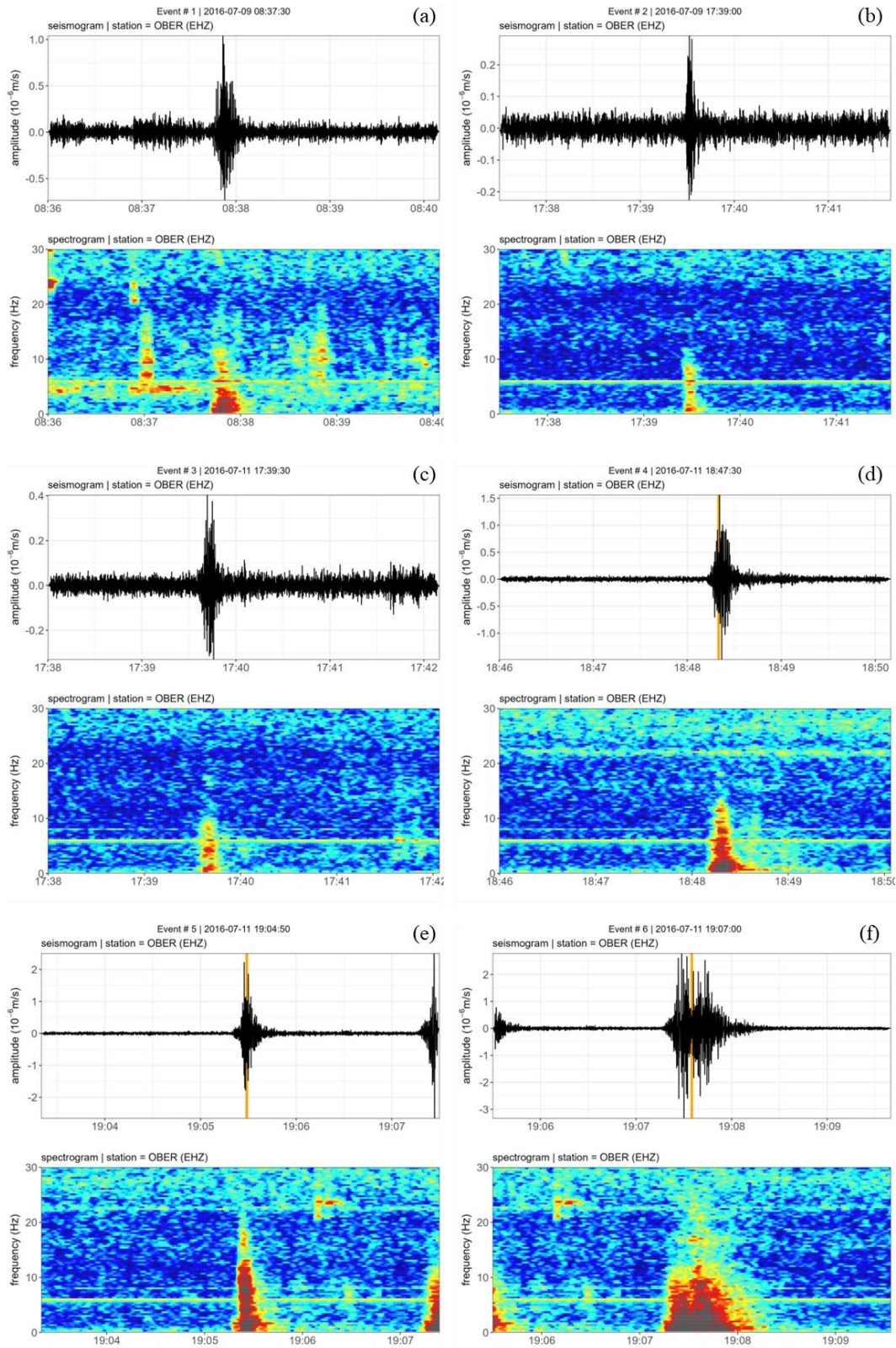
215

Fig. S8 shows the amplitude of the seismic signal and the spectrogram covering all frequencies up to 30 Hz, for each sub-event at the closest station (OBER).

220

225





**Figure S8.** 2016 cliff-fall precursory sub-event. Top image displays the amplitude of the seismic signal. Bottom image displays the spectrogram covering all frequencies up to 30 Hz. a) and b) are events 1 and 2 recorded the 09.07.2016, while c), d) and e) are recorded the 11.07.2016 with decreasing time between events until the final detached (f) sub-event 6, at 19:07 h.

## References

- Akca, D.: Co-registration of Surfaces by 3D Least Squares Matching, *Photogrammetric Eng Remote Sens*, 76, 307–318, <https://doi.org/10.14358/pers.76.3.307>, 2010.
- 235 Dietze, M.: The R package eseis – a comprehensive software toolbox for environmental seismology, *Earth Surf. Dynam*, 1–28, <https://doi.org/10.5194/esurf-2017-75>, 2018.
- Hirschmüller, H.: Stereo Processing by Semiglobal Matching and Mutual Information, *Ieee T Pattern Anal*, 30, 328–341, <https://doi.org/10.1109/tpami.2007.1166>, 2008.
- James, L. A., Hodgson, M. E., Ghoshal, S., and Latiolais, M. M.: Geomorphic change detection using historic maps and DEM differencing: The temporal dimension of geospatial analysis, *Geomorphology*, 137, 181–198, <https://doi.org/10.1016/j.geomorph.2010.10.039>, 2012.
- 240 Kanai, K., Yamabe, K., and Habasaki, A.: Study of the attenuation of seismic waves, in: *Proceedings of the Eighth World Conference on Earthquake Engineering, San Francisco, Prentice-Hall*, 2, 273–280, [https://www.iitk.ac.in/nicee/wcee/eighth\\_conf\\_California/#Volume\\_II](https://www.iitk.ac.in/nicee/wcee/eighth_conf_California/#Volume_II), last access: 18.01.2024, 1984.
- 245 Le Roy, G., Helmstetter, A., Amitrano, D., Guyoton, F., and Roux-Mallouf, R. L.: Seismic Analysis of the Detachment and Impact Phases of a Rockfall and Application for Estimating Rockfall Volume and Free-Fall Height, *J Geophys Res Earth Surf*, 124, 2602–2622, <https://doi.org/10.1029/2019jf004999>, 2019.
- Wheaton, J. M., Brasington, J., Darby, S. E., and Sear, D. A.: Accounting for uncertainty in DEMs from repeat topographic surveys: improved sediment budgets, *Earth Surf Processes*, 35, 136–156, <https://doi.org/10.1002/esp.1886>, 2010.
- 250